Journal of Advanced Ceramics
先进陶瓷
ISSN 2226-4108
CN 10-1154/TQ
清华大学出版社 Tsinghua University Press
SciOpen

J Adv Ceram 2026, **15**: 9221342

https://doi.org/10.26599/JAC.2026.9221342

Research Article

A novel ultrathin nanocrystalline CeO_2 coating achieving high hydrogen permeation barrier performance

Huayu Yang[1], Siyu Gong[1], Shaojie Mo[1], Xinyun Wang[1,*], Heping Li[1,2,*]

[1] *State Key Laboratory of Materials Processing and Die & Mould Technology, School of Materials Science and Engineering, Huazhong University of Science and Technology, Wuhan 430074, China*

[2] *Shenzhen Huazhong University of Science and Technology Research Institute, Shenzhen 518057, China*

* Corresponding authors.

E-mails: X. Wang, wangxy_hust@hust.edu.cn;

H. Li, liheping@hust.edu.cn

Received: April 4, 2026; Revised: June 12, 2026; Accepted: July 3, 2026

Abstract

Hydrogen embrittlement is a serious issue faced by the structural metal materials in hydrogen infrastructures. Developing protective coatings as efficient hydrogen permeation barriers is an urgent need. Here, we report a new nanocrystalline CeO_2 coating with a thickness of ~40 nm successfully fabricated via the coordination-assisted deposition method. By optimizing the annealing condition, the resultant CeO_2 coating has a uniform and dense structure, albeit with a high density of dislocations and grain boundaries. Its hydrogen permeation barrier performance was evaluated by a gas-driven deuterium permeation test, achieving an ultra-low permeability of 1.64×10^{-15} $mol\cdot m^{-1}\cdot s^{-1}\cdot Pa^{-1/2}$ at 500 ℃, three orders of magnitude lower than that of the stainless steel. The corresponding hydrogen permeation reduction factor (PRF) reaches an ultrahigh value of 2355, which is 4 ~ 75 times that of the other oxide nano-coatings such as ZrO_2, Al_2O_3, Cr_2O_3, and Er_2O_3. The intrinsic hydrogen diffusion mechanism in the single crystal coating is revealed by first-principles calculations. In the polycrystal coating, the dense dislocation and boundary contained nanocrystalline structure not only provides abundant hydrogen traps but also prolongs the diffusion pathway to effectively impede hydrogen permeation. This study demonstrates the great potential of CeO_2 as a new type of hydrogen resistant material and most importantly, the roles of microstructure in the design of ultrathin hydrogen permeation barriers with high performance.

Keywords

Hydrogen permeation barrier, Coating, CeO_2, Coordination-assisted deposition method, Ceramic material.

1. Introduction

With the rapid rise in global energy demand, excessive dependence on fossil fuels has resulted in severe environmental challenges, necessitating a shift toward sustainable energy solutions [1]. In this context, hydrogen, as a clean and efficient energy carrier, is regarded as a pivotal component of future energy source [2]. The development and utilization of hydrogen energy not only helps reduce reliance on fossil fuels but also promotes the better energy infrastructures and the sustainable development of the environment [3].

In contemporary energy technologies and nuclear engineering, hydrogen (H), deuterium (D), and tritium (T) function as indispensable reactants and energy carriers, particularly within nuclear fusion reactors and hydrogen storage systems. However, the high permeability of these light elements can lead to hydrogen embrittlement in structural materials, shortening their service life and potentially causing radioactive contamination [4]. Therefore, enhancing the protective properties of materials, especially under extreme conditions, i.e., radiation and high temperature, has thus become a critical area of research. Currently, the application of low-permeability coatings on structural materials is considered a promising solution [5]. Ceramic materials, such as Al_2O_3 [6, 7], Cr_2O_3, Y_2O_3 [8, 9], Er_2O_3 [10, 11], and ZrO_2 [12], are widely used as hydrogen permeation barrier coatings due to their low hydrogen permeability, high strength, and high-temperature resistance. However, these coatings are prone to cracking, delamination, or phase transformation under high-temperature conditions, compromising their hydrogen barrier performance. Additionally, optimizing coating thickness is challenging, as excessive thickness can induce thermal

stress, while insufficient thickness may fail to provide adequate hydrogen permeation resistance. Thus, exploring novel hydrogen barrier coatings and investigating the hydrogen permeation behavior and mechanisms of these materials will offer new directions to overcome the limitations in design of the state-of-the-art hydrogen permeation barriers.

Compared with traditional hydrogen barrier coatings, nanocrystalline coatings offer remarkable advantages in hydrogen resistance due to their unique microstructures [13]. Firstly, the smaller grain sizes and higher grain boundary density significantly increase the complexity of diffusion pathways, extending the permeation path of hydrogen atoms and substantially reducing permeability [14, 15]. Secondly, the nanocrystalline structures can effectively disperse thermal stress, mitigating the risk of cracking caused by stress concentration while enhancing the mechanical properties and thermal stability of the coatings [16]. Rare earth oxides (e.g., CeO_2, La_2O_3) have shown great potential in various applications such as photoelectrodes, thermal barrier coatings, and piezoelectric ceramics, due to their unique electronic structures and high chemical stability [17-19]. Notably, cerium (Ce) stands out as the most abundant rare-earth element in the Earth's crust, with a natural abundance even exceeding that of common base metals such as copper. Consequently, Ce-based coatings enable cost-effectiveness and strategic sustainability for industrial large-scale application. However, the hydrogen permeation barrier performance of these coatings has been scarcely reported, leaving their hydrogen diffusion behavior a mystery.

Herein, we propose a novel and facile strategy for fabricating ultrathin, highly dense, and uniform CeO_2 nanocrystalline coating, and investigate its hydrogen permeation

barrier performance and mechanism. A 40 nm thick CeO_2 coating with a rather dense structure was successfully fabricated on a stainless steel substrate by the coordination-assisted deposition method. Its microstructure and morphology were found to highly depend on the annealing conditions of the as-deposited coating, which impact the hydrogen permeation resistance. When annealed at an optimized temperature, the CeO_2 coating exhibits an exceptional hydrogen barrier performance, with its hydrogen permeation reduction factor (PRF) achieving as high as 2355, a considerable value that has not been reported in nanometer-thick coatings before. Interestingly, large amount of grain boundaries and dislocation network within the CeO_2 coating were observed by SEM and cross-sectional TEM. Moreover, high temperature annealing was performed to observe the effects of microstructure change on hydrogen permeation, allowing us to fathom the correlation between the microstructure features and the hydrogen barrier performance. Furthermore, first-principles calculations were performed to reveal the underlying mechanism of the exceptional hydrogen permeation barrier performance of this ultrathin CeO_2 coating. The findings in this work show CeO_2 as the promising hydrogen barrier material, and also shed light on fabricating nanometer-thick coatings with high hydrogen permeation barrier performance.

2. Materials and Methods

2.1 Materials

Polished 321 stainless steel (Cr 18%, Ni 10%, Mn 2%, Si 1%, balanced by Fe) was used as a substrate for coating deposition due to its outstanding thermal stability and chemical resistance [19]. Cerium(III) nitrate hexahydrate ($Ce(NO_3)_3 \cdot 6H_2O$, purity ≥

99.99%) and isopropanol (purity ≥ 99.7%) were purchased from Macklin Biochemical Co., Ltd. (China). Polyacrylic acid (PAA, average Mw ≈ 1800, purity ≥ 99%) was supplied by Aladdin Reagent Co., Ltd. (China). All chemicals were of analytical grade or higher and used as received without further purification.

2.2 Preparation of nanocrystalline CeO_2 coatings

Nanocrystalline CeO_2 coatings were prepared via a coordination-assisted deposition method. In this process, cerium ions coordinate with carboxyl groups provided by polyacrylic acid in isopropanol solvent, forming a stable precursor solution [20]. The coordination and subsequent thermal decomposition reactions are summarized as

$$Ce(NO_3)_3 + nPAA \rightarrow Ce(PAA)_n \quad (1)$$

and

$$Ce(PAA)_n + O_2 \xrightarrow{\Delta} CeO_x + nCO_2\uparrow + nH_2O. \quad (2)$$

Polyacrylic acid was first dissolved in isopropanol, and then cerium nitrate hexahydrate was introduced into the solution to yield a molar ratio of carboxylic groups (-COOH) to Ce^{3+} ions of approximately 3.5 : 1. The mixture was further stirred until a clear and homogeneous sol was obtained. The solution was deposited on the 321 stainless steel surface by dip coating at a controlled withdrawal speed of 300 μm/s under an ambient environment. After being dried at 95 °C, the as-deposited films were subjected to heat treatment in air at 600-700 °C for 1 h to decompose the organic ligands and crystallize CeO_2.

2.3 Structure and morphology characterization

Thermogravimetric and differential scanning calorimetry (TG-DSC, STA449F3,

NETZSCH, Germany) were conducted to analyze the thermal behavior and decomposition of precursor species. Crystalline structures were identified using X-ray diffraction (XRD, D8 ADVANCE, Bruker, Germany) with Cu Kα radiation. Surface morphology and microstructure of the coatings were examined using field-emission scanning electron microscopy (FE-SEM, Zeiss Sigma 300, Germany) and atomic force microscopy (AFM, SPM-9700, Shimadzu, Japan). Cross-sectional structure and nanocrystallite distribution were further observed via transmission electron microscopy (TEM, Tecnai G2 F20, FEI, USA), while the coating thickness was measured simultaneously. Raman spectroscopy (LabRAM HR800, Horiba Jobin Yvon, France) was used to detect lattice distortions and defect-related features. Electron paramagnetic resonance (EPR, Bruker E500-10/12, Germany) was employed to probe oxygen vacancy concentrations, while surface chemical states and element valence were analyzed by X-ray photoelectron spectroscopy (XPS, AXIS-ULTRA DLD-600W, Shimadzu-Kratos, Japan).

2.4 Hydrogen permeation resistance measurement

As one of the isotopes of hydrogen, deuterium was selected for gas permeation testing, because of tritium's radioactivity and the interference of atmospheric hydrogen. A deuterium permeability test system, as described in Ref. [13], was employed, with the sample positioned between the upstream and downstream chambers. Prior to measurement, both chambers were evacuated to a high vacuum ($<10^{-5}$ Pa) using vacuum pumps. Deuterium gas was then introduced into the upstream chamber to maintain a certain pressure of 40 kPa. Driven by the pressure gradient, deuterium permeated through the sample into the downstream chamber, where the flux was detected. During

the testing, samples were heated to a temperature ranging from 400 °C to 500 °C, closely approximating the actual operating conditions of hydrogen permeation barriers in nuclear fusion reactors. The permeability was calculated following the method described in Ref. [21]. The diffusion of hydrogen isotopes follows Fick's laws, expressed as

$$J = -D\frac{\partial C}{\partial x}, \qquad (3)$$

$$\frac{\partial C}{\partial t} = \frac{\partial}{\partial x}\left(\mathrm{D}\frac{\partial C}{\partial x}\right), \quad (4)$$

where C represents the concentration of the hydrogen isotope dissolved in the sample; J represents the diffusion flux, denoting the quantity of the substance diffusing across a unit of area per unit of time; D represents the diffusion coefficient of the hydrogen isotope.

The temperature dependence of the diffusion coefficient is described by the Arrhenius equation:

$$D = D_0 \exp\left(-Q_D/RT\right) \quad (5)$$

where Q_D denotes the diffusion activation energy, and D_0 is the diffusion constant. The diffusion activation energy represents the energy barrier that must be overcome during the migration of hydrogen isotopes. A higher diffusion activation energy indicates a stronger binding force between the material and the hydrogen isotopes, impeding their diffusion and thereby reducing permeability.

The permeation rate of hydrogen isotopes is quantitatively described by the flux J under steady-state conditions:

$$J = \frac{P\mathrm{p}^n}{\mathrm{d}} \quad (6)$$

$$P = \frac{J\mathrm{d}}{\mathrm{p}^n} \quad (7)$$

where J is the hydrogen permeation flux (mol $m^{-2} \cdot s^{-1}$); P is the permeation rate (mol $m^{-1} \cdot s^{-1} \cdot Pa^{-n}$); p is the upstream gas pressure (Pa); d is the sample thickness (m); and n reflects the hydrogen diffusion model. The extensive gas-driven permeation measurements were performed under a sequence of upstream deuterium driving pressures (20, 40, 60, and 80 kPa) at 500 °C [22]. By analyzing the permeation flux as a function of pressure (Fig. S1), the linear fitting yielded an n value of 0.56 for the CeO_2-coated sample.

The Deuterium Permeation Reduction Factor (PRF) is an important indicator for evaluating hydrogen permeation barrier performance, defined as the ratio of the permeability of the substrate and coating sample:

$$PRF = \frac{P_{substrate}}{P_{coating}} \quad (8)$$

where $P_{substrate}$ and $P_{coating}$ represent the permeability of the substrate and coating samples, respectively.

2.5 First-principles calculations for hydrogen diffusion

First-principles calculations based on Density Functional Theory (DFT) were performed using the VASP software to investigate the interactions between hydrogen and the CeO_2 lattice structures [23]. Owing to the strong on-site Coulomb interaction of localized Ce 4f electrons in CeO_2, which are not well described by conventional DFT, the DFT+U method was adopted with a Hubbard U value of 4.5 eV applied to the Ce 4f states [24]. The simulations focused on calculating the diffusion barriers along different pathways within the CeO_2 lattice. The initial step involved optimizing the CeO_2 crystal structure to identify the most thermodynamically favorable adsorption sites for hydrogen atoms. Based on the optimized initial and final configurations,

hydrogen diffusion energy barriers were determined via transition state calculations. All calculations employed a plane-wave basis set with an energy cutoff of 500 eV. The exchange-correlation energy was treated using the PBEsol functional within the generalized gradient approximation (GGA). Gaussian smearing was used for electronic state occupation (ISMEAR = 0, SIGMA = 0.05 eV), with a self-consistent field (SCF) energy convergence threshold of 1 $\times 10^{-7}$ eV. Ionic relaxations were conducted using the conjugate gradient algorithm (IBRION = 2) with a maximum of 300 steps, where only atomic positions were optimized (ISIF = 2) and the force convergence criterion was set to -0.02 eV/Å. The Brillouin zone was sampled using the Monkhorst-Pack scheme with a grid spacing of 0.040 $Å^{-1}$ and zero symmetry shift, ensuring uniform coverage and accurate resolution of the electronic structure. CeO_2 adopted a cubic fluorite structure with space group $Ia\bar{3}$ and a lattice parameter of $a = b = c = 10.604$ Å. In consideration of its crystallographic symmetry and the required computational precision, a 2×2×2 K-point mesh was applied.

3. Results and discussion

We successfully fabricated nanocrystalline CeO_2 coatings via a coordination-assisted deposition method based on a sol-gel strategy. The specific preparation process is schematically depicted in Fig. 1a. In this approach, organic ligands form stable coordination complexes with metal ions in solution, allowing precise control over precursor solubility, hydrolysis kinetics, and deposition behavior. Compared to conventional sol-gel techniques, this method offers several advantages, including molecular-level control of coating composition, tunable film thickness through

precursor concentration, and a simple, low-cost, and scalable fabrication process. In this study, cerium nitrate hexahydrate served as the cerium source, polyacrylic acid provided carboxyl functional groups for coordination, and isopropanol was used as the reaction solvent. The resulting homogeneous solution was applied to polished 321 stainless steel substrates via dip-coating. The subsequent annealing process decomposed the organic components, yielding uniform and phase-pure nanocrystalline CeO_2 coatings.

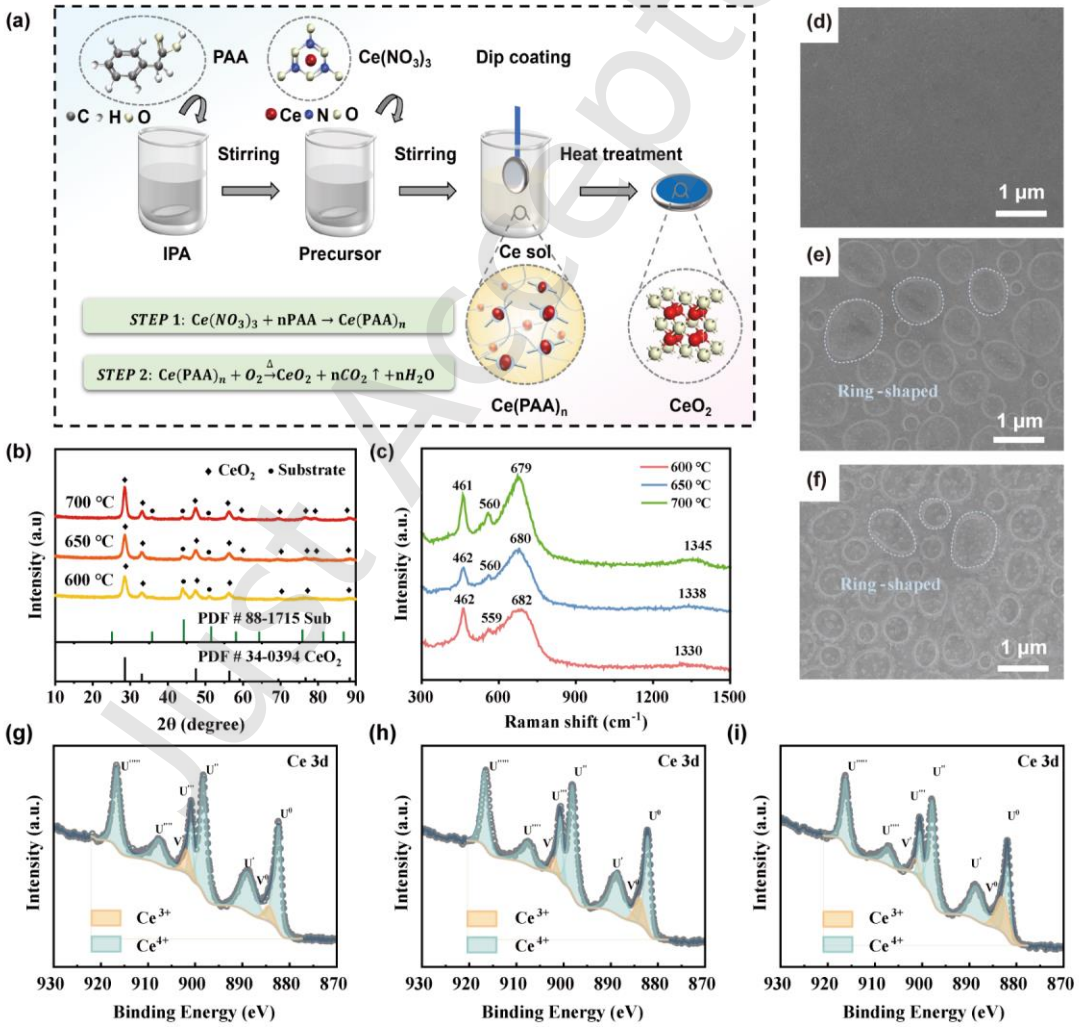

Fig. 1 Fabrication and characterization of nanocrystalline CeO_2 coatings: (a) Schematic illustration of the preparation process for CeO_2 coatings; (b) XRD patterns of CeO_2 coatings annealed at different temperatures; (c) Raman spectra; (d) SEM surface morphology and microstructure features (grains and grain size) of CeO_2 coatings annealed at 600 °C, (e) at 650 °C, and (f) at 700 °C; (g) Ce

3d XPS spectra (600 °C); (h) Ce 3d XPS spectra (650 °C); (i) Ce 3d XPS spectra (700 °C).

Grazing-incidence X-ray diffraction (GIXRD) patterns confirm the formation of crystalline CeO_2 over a temperature range from 600 °C to 700 °C. As seen in Fig. 1b, the diffraction peaks correspond well to the fluorite-type cubic structure of CeO_2, with no evidence of secondary phases. The intensities of the peaks gradually increase with annealing temperature, reflecting enhanced crystallinity. Meanwhile, no shift in peak position is detected, suggesting that the lattice parameters remain stable and no phase transformation occurs during annealing. The average grain size, derived from the Scherrer equation, is presented in Fig. S2, increasing from 14 nm at 600 °C to 24 nm at 650 °C, and reaching 30 nm at 700 °C.

As shown in Fig. 1c, the Raman spectra collected at different annealing temperatures show that the F_{2g} symmetric stretching mode remains centered at approximately 461 cm^{-1} across all annealing temperatures, suggesting excellent thermal stability of the cubic fluorite phase without evident phase transformation [25]. The prominent scattering features of the spectra are meticulously assigned as follows: First, the dominant, sharp symmetry band centered at ~461 cm^{-1} represents the active F_{2g} symmetric stretching mode characteristic of the ideal cubic fluorite CeO_2 structure. Second, the distinct, broad shoulder features emerging within the 560-680 cm^{-1} region, specifically resolved at ~560 cm^{-1} and ~679 cm^{-1}, are identified as defect-induced longitudinal optical bands (D modes). These features are strictly tied to the breaking of local lattice translation symmetry caused by the formation of oxygen vacancy clusters that balance the thermal reduction of Ce^{4+} to Ce^{3+}. Concurrently, the Raman spectra reveal a gradual enhancement of these defect-related features with increasing

temperature, indicating a temperature-dependent evolution of the lattice structure and an upward trend in oxygen vacancy concentration [26]. This evolution is further supported by Fig. S3, where EPR spectra show a clear enhancement in signal intensity corresponding to paramagnetic oxygen vacancies as the annealing temperature rises [27]. Lastly, the broad scattering envelope near ~1330 cm^{-1} represents a second-order Raman scattering mode. The progressive blue-shift and intensity evolution of this ~1330 cm^{-1} peak directly reflect the accumulation of severe localized lattice distortion and internal mechanical strain within the CeO_2 lattice during grain coalescence.

The surface morphology of the coatings at elevated temperature was further characterized by Scanning Electron Microscopy (SEM). As shown in Figs. 1d-e, with the annealing temperature increasing from 600 °C to 650 °C, the grains begin to coarsen alongside the emergence of bubble-like structures driven by enhanced atomic diffusion. This trend becomes more pronounced at 700 °C (Fig. 1f), where severe grain agglomeration and large aggregated grains are observed, indicating significant temperature-induced grain coalescence. The ring-like feature observed by SEM was found to be related to certain grains aligned along the ridge of the surface roughness, not any new microstructure, possibly a result of surface energy promoted morphology change.

To investigate the effects of annealing temperature on the composition and defect behavior of CeO_2 coatings, X-ray photoelectron spectroscopy (XPS) was employed to examine the evolution of their valence states. Typically, the Ce 3d XPS spectrum of CeO_2 exhibits eight characteristic peaks, resulting from the spin-orbit splitting of the Ce 3d level [28, 29]. Specifically, spectra were calibrated to C 1s at 284.8 eV. During

fitting, doublet and satellite peak separations were fixed to reference values, while component FWHMs within the same oxidation state were set equal and constrained within 1.2-1.8 eV. As shown in Figs. 1g-i, all samples display the coexistence of Ce^{4+} and Ce^{3+} oxidation states. The spectral features are dominated by Ce^{4+} signatures, specifically the characteristic u'''/v''', u''/v'' and u/v peaks, while distinct Ce^{3+} peaks (u'/v' and u^0/v^0) are consistently observed. Of particular significance is the progressive enhancement of the u^0/v^0 peak intensity with increasing annealing temperature, which provides direct evidence for thermally promoted reduction of Ce^{4+} to Ce^{3+}. This valence transition is accompanied by the formation of oxygen vacancies to maintain charge neutrality within the crystal lattice, as governed by the Kröger-Vink notation [30]. The corresponding defect reaction can be expressed as:

$$Ce_2O_3 \xrightarrow{2CeO_2} 2Ce'_{ce}+3O_O+V''_O \quad (9)$$

The O1s spectra further corroborate this phenomenon (Figs. S4a-c). The O1s peak is deconvoluted into two components: the lattice oxygen peak at 529.5 eV (O_α) and the oxygen vacancy-associated adsorbed oxygen peak at 532 eV (O_β). The contribution of surface-adsorbed oxygen was negligible and therefore excluded from the analysis. The oxygen vacancy concentration (O_v) was quantified using the ratio $O_\beta/(O_\alpha + O_\beta)$. The results show that the oxygen vacancy concentration exhibits an upward trend with increasing annealing temperature, which is in good agreement with the EPR results discussed above. Overall, despite the deviation from stoichiometry, the dominant phase of the CeO_2 coating maintains a crystalline cubic fluorite structure.

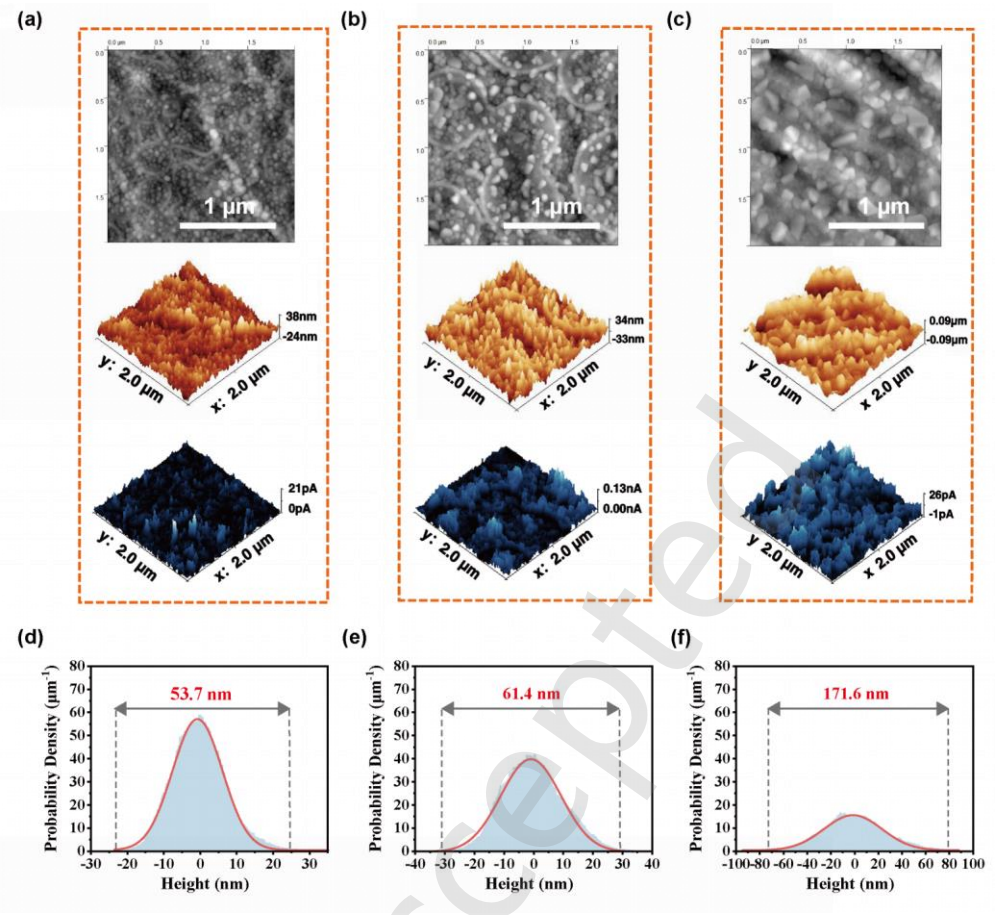

Fig. 2 AFM characterization of nanocrystalline CeO_2 coatings at different annealing temperatures: (a) AFM surface morphology and microstructure of CeO_2 coating annealed at 600 °C, (b) at 650 °C, and (c) at 700 °C; (d) Surface roughness height distribution density of CeO_2 coating annealed at 600 °C, (e) at 650 °C, and (f) at 700 °C.

The microstructural surface quality of CeO_2 coatings annealed at three different temperatures was further investigated using AFM, as shown in Figs. 2a-c. The figures illustrate that the surface morphological features of the CeO_2 coating evolve progressively with increasing annealing temperature. To quantitatively characterize this evolution, statistical analysis of surface height distribution density was performed. It reveals that as the annealing temperature increases from 600 °C to 700 °C, the peak height expands from 53.7 nm (Fig. 2d) to 61.4 nm (Fig. 2e) and ultimately to 171.6 nm (Fig. 2f), reflecting a significant increase in surface roughness caused mainly by the

grain coarsening.

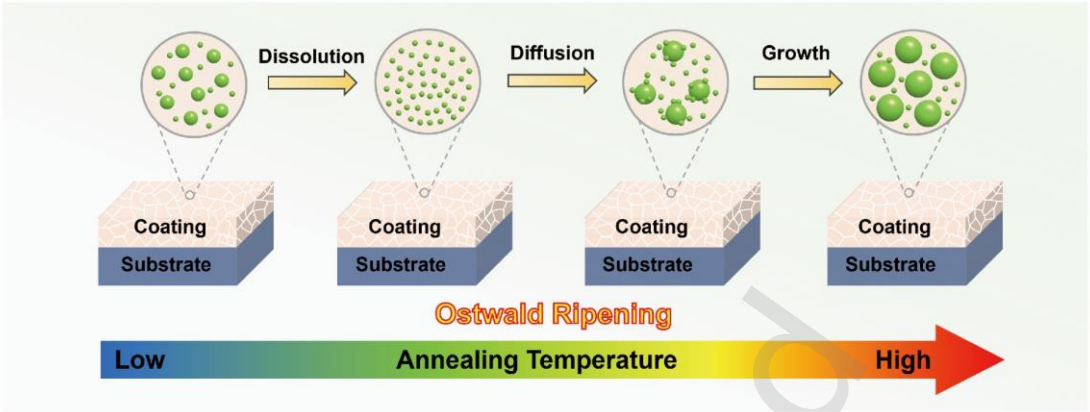

Fig. 3 Schematic illustration of Ostwald ripening mechanism for CeO_2 grain growth.

This observed roughness evolution primarily stems from grain coarsening driven by the Ostwald ripening mechanism, which is schematically depicted in Fig. 3. Specifically, smaller particles exhibit reduced stability due to their inherently higher surface energy resulting from pronounced curvature effects, consequently undergoing preferential dissolution [31, 32]. The liberated species subsequently undergo diffusional transport and heterogeneous redeposition onto larger crystalline domains, thereby driving progressive grain growth. Concurrently, elevated temperatures significantly enhance atomic mobility, which in turn facilitates both surface and grain boundary diffusion. This thermal activation effect not only accelerates grain coarsening but can also induce grain boundary migration and structural reconstruction, ultimately leading to substantial morphological transformations of the coating surface [33]. Interestingly, this thermal reconstruction and surface Ostwald ripening behavior is not just confined to the oxide coating but is also concurrently active within the metallic substrate under thermal treatment. As evidenced by the control experiments on bare, polished steel substrate (Figs. S5a-b), the substrate surface height variations expand from ~47 nm at

600 °C to ~60 nm at 700 °C due to thermal grain growth. This leads to the observation that the overall height distribution of the coating sample is considerably larger than the film thickness.

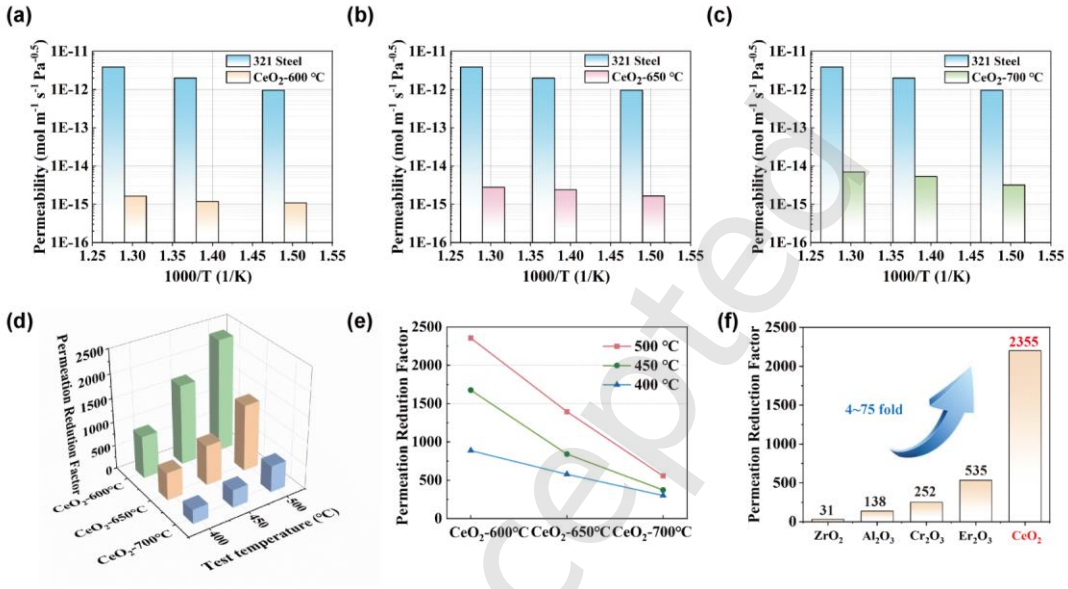

Fig. 4 Hydrogen barrier performance of nanocrystalline CeO_2 coatings at different annealing temperatures: (a) Hydrogen resistance comparison: 600 °C coating vs. 321SS substrate at different permeation temperatures, (b) 650 °C coating vs. 321SS substrate at different permeation temperatures, and (c) 700 °C; (d) Hydrogen resistance of differently annealed coatings across permeation temperatures; (e) Annealing temperature dependence of hydrogen resistance at various permeation temperatures; (f) Comparison of permeation reduction factor between CeO_2 and other single-oxide coatings at a permeation temperature of 500 ℃.

Equation (5) illustrates that higher temperatures accelerate deuterium diffusion, while lower temperatures slow the process. The permeation rate of deuterium increases proportionally with temperature. For instance, the permeation rates of a 321 stainless steel substrate at 400 °C, 450 °C, and 500 °C are 9.57×10^{-13} mol s^{-1} m^{-1} $Pa^{-1/2}$, 1.99×10^{-12} mol s^{-1} m^{-1} $Pa^{-1/2}$, and 3.86×10^{-12} mol s^{-1} m^{-1} $Pa^{-1/2}$, respectively, representing a 50% average increase in permeation rate for every 50 °C increment. Figures 4a-c present the

temperature-dependent deuterium permeation rates (400-500 °C) for nanocrystalline CeO_2 coatings annealed at three different temperatures, with corresponding data for the 321 stainless steel substrate shown in Fig. S6. Notably, the CeO_2 coatings demonstrate 2-3 orders of magnitude lower permeation rates compared to the bare substrate. At 500 °C, the measured permeabilities of CeO_2-600 °C, CeO_2-650 °C, and CeO_2-700 °C coatings were 1.64×10^{-15} mol s^{-1} m^{-1} $Pa^{-1/2}$ (Fig. 4a), 2.78×10^{-15} mol s^{-1} m^{-1} $Pa^{-1/2}$ (Fig. 4b), and 6.94×10^{-15} mol s^{-1} m^{-1} $Pa^{-1/2}$ (Fig. 4c), respectively. Based on Equation (8), the PRF values of CeO_2-600 °C, CeO_2-650 °C, and CeO_2-700 °C show a gradual decrease (Fig. 4d), with values of 2355, 1675, and 886, respectively. This indicates that the CeO_2 nanocrystalline coating annealed at 600 °C exhibits the best hydrogen barrier performance with the highest hydrogen permeation resistance among these samples. As shown in Fig. 4e, the *PRF* values of all samples exhibit an increasing trend as the permeation temperature increases, similar to our previous observation in other oxide coatings [34]. This phenomenon is due to the significant increase in permeability of the steel substrate at higher temperatures. As the permeability of the coating changes slightly with rising permeation temperature, the PRF value increases accordingly. As a comparison, we also prepared other nanometer-thick oxide coatings by the sol-gel method, such as ZrO_2, Al_2O_3, Cr_2O_3, and Er_2O_3. It is worth mentioning that the hydrogen permeation barrier performance of CeO_2 coating greatly exceeds that of other oxide materials, with its PRF value 75 times that of ZrO_2, 17 times that of Al_2O_3, 9 times that of Cr_2O_3, and 4 times that of Er_2O_3. The ZrO_2, Al_2O_3, Cr_2O_3 and Er_2O_3 coatings used as reference samples here were fabricated in our laboratory with the same coating processes and annealing conditions as the CeO_2 coating. The hydrogen

permeation resistance of these coatings was further evaluated under the identical permeation testing parameters. Consequently, the observed variation in PRF directly underscores the intrinsic superiority of CeO_2 material in impeding hydrogen permeation. This great enhancement in hydrogen permeation barrier performance is owing to the unique microstructure and electronic structure of the CeO_2 coating, as revealed by the subsequent analyses.

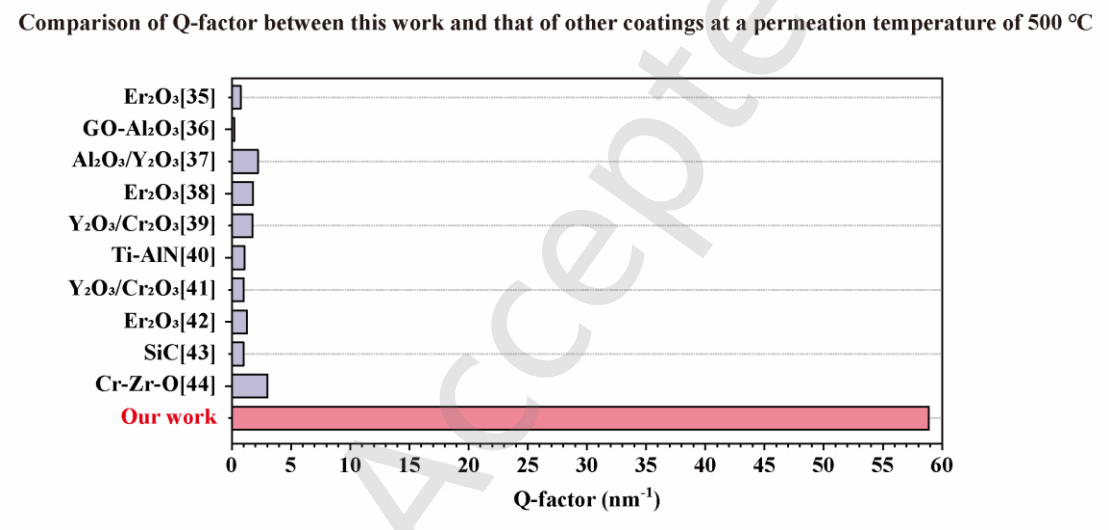

Fig. 5 Comparison of Q-factor between this work and other hydrogen barrier coatings at a permeation temperature of 500 ℃ [35-44].

Here, for the first time, we introduce the quality factor (Q-factor) to quantitatively evaluate the hydrogen barrier efficiency normalized to coating thickness, which characterizes a material's intrinsic ability to suppress hydrogen permeation per unit thickness. It is proposed as an efficiency metric to evaluate the overall hydrogen barrier capability normalized by thickness, rather than to describe the intrinsic physical transport behavior of hydrogen isotopes. This parameter enables a normalized comparison of hydrogen isotope barrier performance across coatings of varying

thicknesses, thereby highlighting materials with superior performance-to-thickness ratios. The Q-factor is defined as:

$$Q = \frac{PRF}{d^{\alpha}} \quad (10)$$

where PRF is the permeation reduction factor, d is the coating thickness, and α is the thickness sensitivity exponent, typically taken as 1 but adjustable when fitting multiple experimental datasets to optimize the linear correlation and more accurately capture the thickness dependence of permeation behavior. In this study, α is set to 1 to evaluate the thickness-normalized permeation resistance.

We calculated the Q-factor of various types of hydrogen permeation barrier coatings, as summarized in Table S1 and Fig. 5. Compared with these previously reported coatings [35-44], the CeO_2 coating developed here exhibits an exceptional Q-factor of 50 nm^{-1}, which is at least an order of magnitude higher than those of conventional hydrogen barrier materials. This remarkable improvement underscores the superior hydrogen barrier performance of the CeO_2 coating presented in this work.

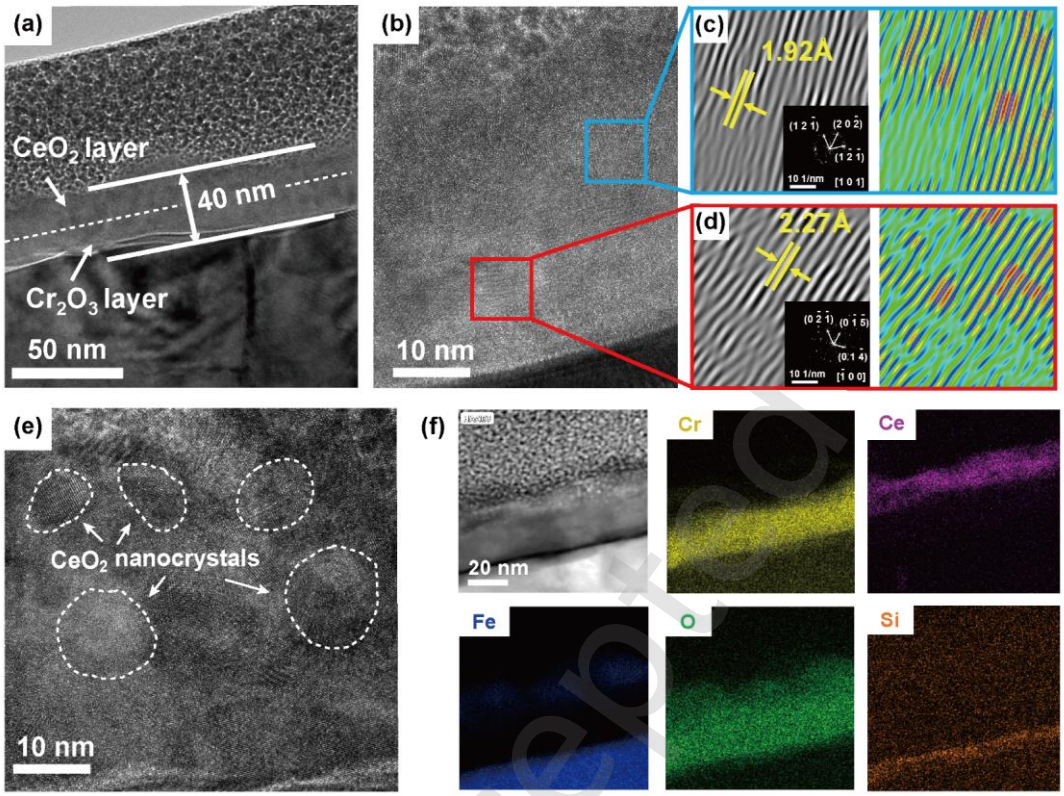

Fig. 6 (a) Bright-field TEM images of the CeO_2 coating annealed at 600 °C; (b) Bright-field TEM images of the CeO_2 coating annealed at 600 °C; (c) HRTEM lattice fringes of CeO_2; (d) HRTEM lattice fringes of Cr_2O_3; (e) High-resolution TEM image of the CeO_2 nanocrystalline structure; (f) EDS elemental mapping of the CeO_2 coating annealed at 600 °C.

The CeO_2 hydrogen barrier coating annealed at 600 °C was further characterized using focused ion beam (FIB) milling in conjunction with transmission electron microscopy (TEM) to investigate its cross-sectional microstructure and interfacial features. Fig. 6a shows a bright-field TEM image of the coating cross-section, indicating that the CeO_2 coating possesses a uniform, continuous, and densely packed polycrystalline nanostructure with a total thickness of approximately 40 nm. From the elemental distribution analysis, the oxygen element is uniformly distributed across the coating, while a slight segregation of Si is observed near the interface (Fig. 6f), possibly originating from the substrate. Notably, Cr diffusion from the stainless steel substrate

into the coating led to the formation of an interfacial Cr_2O_3 layer with an estimated thickness of ~20 nm. This layer results from the in-situ oxidation of diffused Cr during the annealing process, which is anticipated to strengthen the interfacial adhesion of the coating according to our previous findings [45, 46].

Fig. 6b shows a bright-field TEM image of the CeO_2 coating, revealing a dense, fine-grained structure. Two representative regions were selected for high-resolution analysis, corresponding to the CeO_2 and Cr_2O_3 phases, respectively. Figs. 6c-d show high-resolution TEM images of the lattice fringes of the two phases. The interplanar spacing of 1.92 Å is indexed to the (1 -2 -1) planes of cubic CeO_2 along the [1 0 1] zone axis, while the spacing of 2.27 Å corresponds to the (0 1 -4) planes of rhombohedral Cr_2O_3 along the [-1 0 0] zone axis. Selected-area electron diffraction (SAED) further verifies the phase composition. Besides the abundant grain boundaries in the nanograins, interestingly, clear dislocations are observed in the lattice fringe images, especially near grain and phase boundaries, indicating local stress concentrations due to nanoscale grain size. The high density of grain boundaries and dislocations is speculated to enhance the hydrogen permeation resistance by serving as preferential trapping sites for hydrogen isotopes, thereby reducing their mobility while simultaneously increasing the tortuosity of diffusion pathways, and therefore effectively impeding hydrogen isotope transport through the coating [47-49].

However, as the annealing temperature increases from 600 °C to 700 °C, the macro-scale barrier efficiency (PRF) exhibits a progressive decline. From our observations, we could correlate the change in PRF to changes in the microstructures, i.e., grain size and grain boundary, as well as dislocations. Elevated temperature provides sufficient

thermal activation energy to drive grain growth, leading to a marked decrease in grain boundary density. Concurrently, high-temperature exposure inevitably induced a substantial thermal recovery process, during which highly-dense dislocations that characteristically trapped near boundaries underwent rapid rearrangement and annihilation [50, 51]. As the annealing temperature rose further, substantial alterations in surface microstructure and significant coarsening of grain sizes occurred. These changes allow the surviving grain boundaries and dislocation segments to become shortened or reconnect, forming through-thickness penetration pathways that drastically accelerate hydrogen isotope transport. Consequently, the simultaneous reduction of these concurrent trapping and scattering centers collectively diminishes the structural transport barriers, opening up freer diffusion pathways and yielding the observed degradation in barrier performance [52, 53]. Fig. 6e displays a uniform distribution of CeO_2 nanocrystallites within the coating, with their characteristic size of approximately 8~10 nm. This refined grain structure effectively inhibits grain boundary migration, thereby further enhancing the structural stability of the coating.

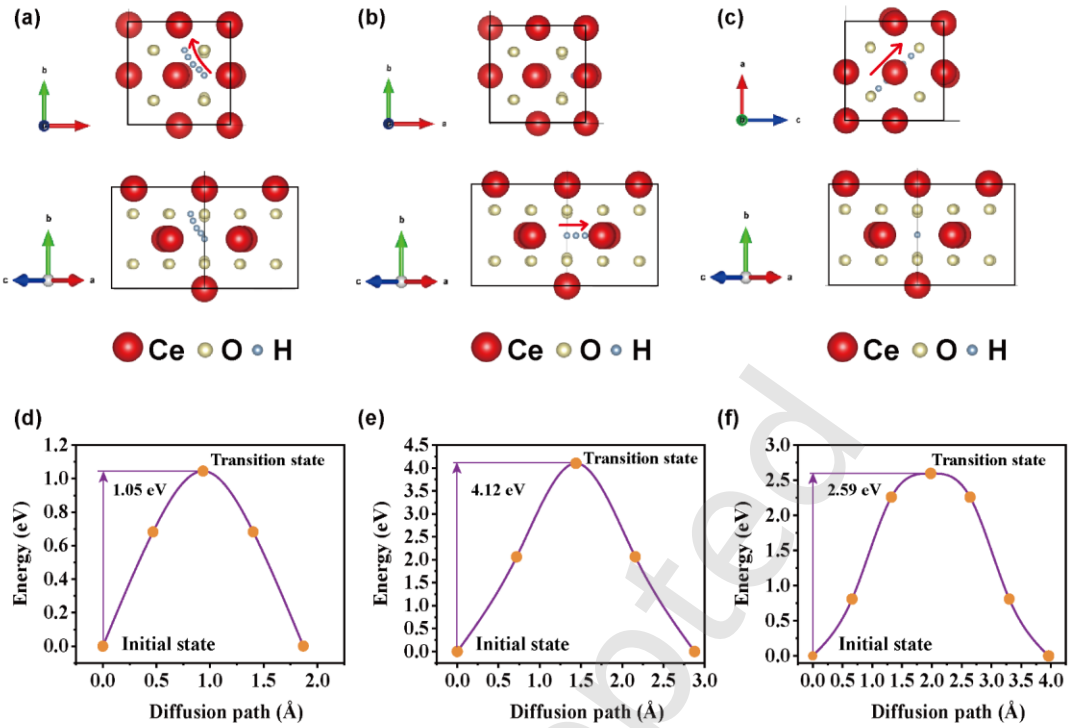

Fig. 7 Hydrogen diffusion mechanism and electronic structure analysis of CeO_2 nanocrystals by DFT calculations: (a) Schematic of hydrogen migration pathway 1 in CeO_2 nanocrystals; (b) Schematic of hydrogen migration pathway 2 in CeO_2 nanocrystals; (c) Schematic of hydrogen migration pathway 3 in CeO_2 nanocrystals; (d) Diffusion activation energy for path 1; (e) Diffusion activation energy for path 2; (f) Diffusion activation energy for path 3.

In the past decade, DFT methods have played a more and more important role in providing insights into the mechanism behind the experimental observations, not only for single-crystal materials but also for polycrystalline structures [54, 55]. To fundamentally elucidate hydrogen diffusion in the nanocrystalline CeO_2 coatings, we employed first-principles density functional theory (DFT) calculations using the Vienna Ab initio Simulation Package (VASP) to construct atomic-scale diffusion models. Transition states along the migration paths were identified using the state-of-the-art climbing image nudged elastic band (CI-NEB) method, in which intermediate images were optimized on the potential energy surface [56-58]. Three representative

diffusion pathways were selected to elucidate the atomic-scale mechanisms of hydrogen transport and their dependence on local crystallographic and electronic environments (Figs. 7a-c). CI-NEB calculations revealed pronounced anisotropy in hydrogen mobility, with diffusion barriers of 1.05 eV (Fig. 7d), 4.12 eV (Fig. 7e), and 2.59 eV (Fig. 7f), respectively. Notably, the lowest barrier of 1.05 eV corresponded to the most thermodynamically favorable pathway, while the substantially higher barriers of 4.12 eV and 2.59 eV were associated with strong localized electronic interactions and structural constraints that significantly hindered hydrogen migration.

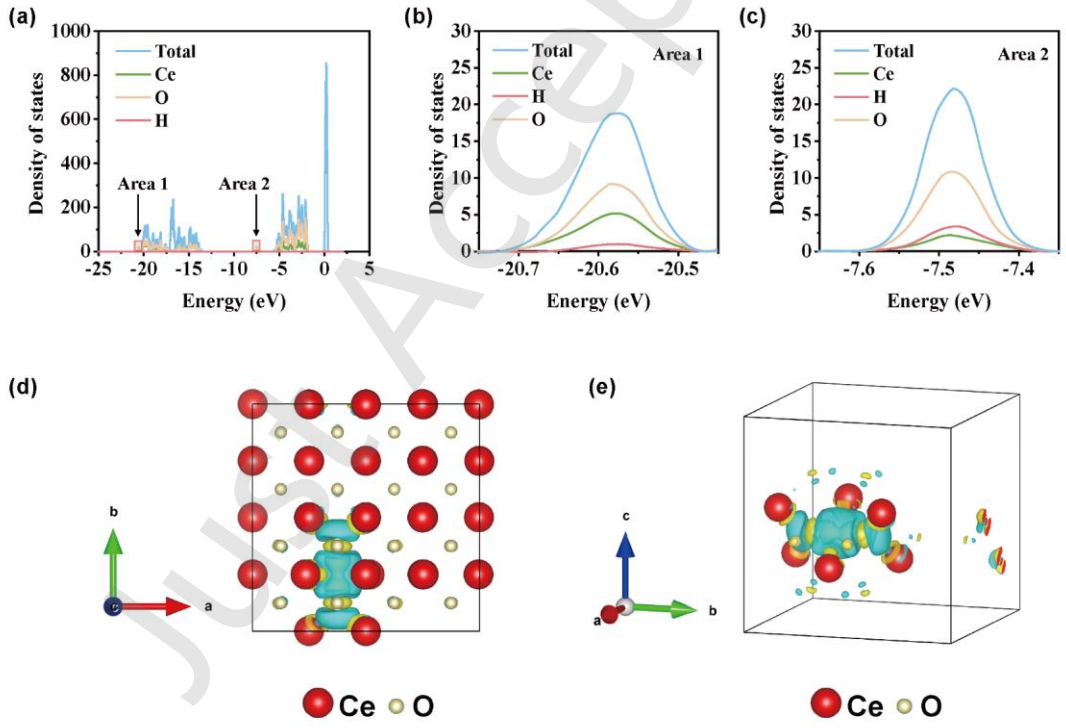

Fig. 8 Hydrogen diffusion mechanism and electronic structure analysis of CeO_2 nanocrystals by DFT calculations: (a) Total density of states (TDOS) plot; (b) Enlarged view of DOS area 1; (c) Enlarged view of DOS area 2; (d)-(e) Differential charge density map, where cyan and yellow colors represent charge depletion and accumulation regions in real space, respectively.

To gain a deeper insight into the electronic origins of these diffusion characteristics, we performed density of states (DOS) calculations. Importantly, the results revealed

pronounced peak overlaps between H 1s, Ce 4f, and O 2p orbitals in specific energy regions (Figs. 8a-c), strongly indicating substantial electron transfer between hydrogen and the surrounding Ce-O matrix. In the pristine CeO_2 lattice, the low electronegativity of Ce (1.12) relative to O (3.44) facilitates strong ionic bonding. Upon introduction of hydrogen (electronegativity = 2.20), partial electron transfer occurs from adjacent oxygen atoms to the hydrogen atom, enabling it to stably localize within the interstitial space framed by Ce and O atoms. This configuration minimizes the system's total energy and enhances electronic coupling between hydrogen and the host lattice.

This mechanism is further supported by differential charge density maps (Figs. 8d-e), which reveal pronounced electron localization when hydrogen occupies the octahedral interstitial sites of the fluorite structure. Clear charge redistribution is observed, with electron density accumulation between hydrogen and adjacent oxygen atoms, accompanied by a depletion near the Ce sites. This electronic rearrangement signifies the formation of a localized bonding state, which imposes a substantial energy penalty for hydrogen migration and effectively traps hydrogen atoms within octahedral sites, thereby suppressing long-range diffusion. Overall, the presence of a 1.05 eV diffusion barrier along the most favorable migration pathway, combined with pronounced charge localization, gives rise to a highly corrugated potential energy landscape that substantially impedes hydrogen transport through the CeO_2 lattice.

4. Conclusions

In summary, the ultrathin nanocrystalline CeO_2 coating with an overall thickness of only 40 nm was successfully fabricated for the first time via the coordination-assisted

deposition method. When annealed at an optimized temperature of 600 °C, the coating had a highly compact surface, uniformly fine-grained microstructure, and a high density of dislocations, which guaranteed its exceptional hydrogen barrier performance. An ultralow deuterium permeability of 1.64×10^{-15} $mol\cdot m^{-1}\cdot s^{-1}\cdot Pa^{-1/2}$ at 500 °C was achieved in the nanocrystalline CeO_2 coating, corresponding to an exceptionally high permeation reduction factor (PRF) of 2355. This hydrogen permeation barrier performance is 4~75 times that of the other oxide materials such as ZrO_2, Al_2O_3, Cr_2O_3, and Er_2O_3. Furthermore, first-principles calculations reveal that the most favorable migration pathway of hydrogen in CeO_2 exhibits an energy barrier of 1.05 eV. Additionally, strong electronic interactions between H and the surrounding Ce-O matrix, arising from the hybridization of H 1s with O 2p and Ce 4f states, further impede hydrogen diffusion. Heat treatment of the films at elevated temperature show the strong correlation between the hydrogen permeation and microstructures, which is caused most likely by the shortening and rewiring of the diffusion pathways formed by dislocation networks and grain boundaries. The remarkable combination of facile fabrication, ultrathin thickness, and high hydrogen permeation resistance highlights the great potential of CeO_2 as high-performance hydrogen permeation barriers in a wide variety of applications, such as nuclear fusion reactors, hydrogen energy, and hydrogen-embrittlement protection in other fields.

Acknowledgment

This work was supported by the National Key Research and Development Program of China (Grant No. 2023YFB3508600), the National Natural Science Foundation of

China (Grant No. 52553007 and 52273224), Guangdong Basic and Applied Basic Research Foundation (Grant No. 2024B1515020045). The authors thank Prof. Zhangcan Yang (Huazhong University of Science and Technology) for providing the software for First-principles calculations, and also thank Analytical and Testing Center of Huazhong University of Science and Technology for support.

Author contributions

Huayu Yang: Investigation, Formal analysis, Writing-original draft. **Siyu Gong:** theoretical calculations, Writing-original draft. **Shaojie Mo:** Formal analysis, Writing-original draft. **Xinyun Wang:** Supervision, Resources. **Heping Li:** Supervision, Conceptualization, Writing-review & editing, Funding acquisition.

Declare of interests

The authors declare that they have no known competing financial interests or personal relationships that could have appeared to influence the work reported in this paper.

Supplementary information

Supplementary materials are available in the online version of the paper.

References

[1] Vogt ETC, Weckhuysen BM. The refinery of the future. Nature 2024, **629**: 295-306.

[2] Zheng L, Zheng Z, Yan Y et al. High hydrogen permeation resistance achieved in a novel (AlCrZr)O ternary oxide nanofilm. J Adv Ceram 2025, **14**: 9221064.

[3] Hossain MK, Hashizume K. A comparative study on the hydrogen dissolution and release behaviors in the zirconate proton conductors by TDS and TMAP4 analysis. J Alloy Compd 2022, **907**: 164436.

[4] Yang HG, Zhan Q, Zhao WW, et al. Study of an iron-aluminide and alumina tritium barrier coating. J Nucl Mater 2011, **417**: 1237-1240.

[5] Zheng Z, Yang Z, Yan Y et al. Effects of internal stress and hydrogen penetration on the performance of Er_2O_3 coatings as hydrogen permeation barriers. ACS Appl Mater Interfaces 2024, **16**: 22471-22481.

[6] Zhu C, Zhang W, Wang L, et al. Effect of thermal cycles on structure and deuterium permeation of Al_2O_3 coating prepared by MOD method. Fusion Eng Des 2020, **159**: 111750.

[7] Huang J, Xie H, Luo L, et al. Preparation and properties of FeAl/Al_2O_3 composite tritium permeation barrier coating on surface of 316L stainless steel. Surf Coat Technol 2020, **383**: 125282.

[8] Wu Y, Li S, He D, et al. Influence of annealing atmosphere on the deuterium permeation of Y_2O_3 coatings, Int J Hydrog Energy 2016, **41**: 10374-10379.

[9] Engels J, Houben A, Rasinski M, et al. Hydrogen saturation and permeation barrier performance of yttrium oxide coatings. Fusion Eng Des 2017, **124**: 1140-1143.

[10] Chikada T, Suzuki A, Kobayashi T, et al. Microstructure change and deuterium permeation behavior of erbium oxide coating. J Nucl Mater 2011, **417**: 1241-1244.

[11] Li Q, Wang J, Xiang Q, et al. Thickness impacts on permeation reduction factor of Er_2O_3 hydrogen isotopes permeation barriers prepared by magnetron sputtering. Int J Hydrog Energy 2016, **41**: 3299-3306.

[12] Wu J, Xie J, He M, et al. Yttria-stabilized zirconia composite coating as barrier to reduce hydrogen permeation into steel. Materials 2024, **17**: 3017.

[13] Zheng Z, Li H, Li F, et al. An efficient PDA/Al_2O_3 nanosheets reinforced ultra-thin ZrO_2 coating with attractive anti-corrosion and deuterium resistance property. Chem Eng J 2022, **450**: 138307.

[14] Hu L, Wei G, Yin R, et al. Significant hydrogen isotopes permeation resistance via nitride nano-multilayer coating. Int J Hydrog Energy 2020, **45**: 19583-19589.

[15] Li M, Zhu Y, Yang C, et al. Enhanced electrochemical hydrogen storage properties of Mg_2NiH_4 by coating with nano-nickel. Int J Hydrog Energy 2015, **40**: 13949-13956.

[16] Li X, Du S, Ma C, et al. Nano-SiO_2 based anti-corrosion superhydrophobic coating on Al alloy with mechanical stability, anti-pollution and self-cleaning properties. Ceram Int 2024, **50**: 9469-9478.

[17] Zheng L, Xu A, Li F et al. Improving hydrogen permeation resistance in ultrathin ZrO_2 coating via Y dopant tuning. ACS Appl Mater Interfaces 2025, **17**: 50011-50023.

[18] Yang W, Wang J, Gao S, et al. Photo-assisted charging of carbon fiber paper-supported CeO_2/MnO_2 heterojunction and its long-lasting capacitance

enhancement in dark. J Adv Ceram 2022, **11**: 1735-1750.

[19] Zhang G, Chen C, Luo D, et al. An advance process of aluminum rich coating as tritium permeation barrier on 321 steel workpiece. Fusion Eng Des 2012, **87**: 1370-1375.

[20] Guo S, Li Y, Li B, et al. Coordination-assisted precise construction of metal oxide nanofilms for high-performance solid-state batteries. J Am Chem Soc 2022, **144**: 2179-2188.

[21] Li F, Zheng Z, Wang X, et al. Horizontally aligned BN nanosheet array for nanometer-thick ZrO_2 coating with greatly enhanced anticorrosion and hydrogen isotope resistance property. Chem Eng J 2022, **440**: 135920.

[22] Young KT, Smith C, Krentz TM, et al. Graphene synthesized by chemical vapor deposition as a hydrogen isotope permeation barrier. Carbon 2021, **176**: 106-117.

[23] Horton MK, Huck P, Yang RX, et al. Accelerated data-driven materials science with the materials project. Nat Mater 2025, **24**: 1522-1532.

[24] Bajaj A, Kulik HJ. Molecular DFT plus U: a transferable, low-cost approach to eliminate delocalization error. J Phys Chem Lett 2021, **12**: 3633-3640.

[25] Li L, Hu G, Lu J, et al. Review of oxygen vacancies in CeO_2-doped solid solutions as characterized by raman spectroscopy. Acta Phys-Chim Sin 2012, **28**: 1012-1020.

[26] Askrabic S, Dohcevic-Mitrovic Z, Kremenovic A, et al. Oxygen vacancy-induced microstructural changes of annealed CeO_{2-x} nanocrystals, J Raman Spectrosc 2012, **43**: 76-81.

[27] Rakhmatullin RM, Morozov OA, Korableva SL, et al. Oxygen vacancies, hydroxyl groups and fluorine ions in the local environment of Yb^{3+} ions doped in

CeO_2 nanoparticles. Ceram Int 2024, **50**: 46516-46521.

[28] Yin Z, Mao Y, Shi S, et al. Solution combustion synthesis of high-entropy rare earth oxide $Ce_{0.2}La_{0.2}Gd_{0.2}Y_{0.2}Lu_{0.2}O_{1.6}:Eu^{3+}$ phosphor with intense blue-light excitable red emission for solid-state lighting. J Adv Ceram 2024, **13**: 1852-1860.

[29] Wang K, Chang Y, Lv L, et al. Effect of annealing temperature on oxygen vacancy concentrations of nanocrystalline CeO_2 film. Appl Surf Sci 2015, **351**: 164-168.

[30] Kumar N, Patterson EA, Froemling T, et al. Defect mechanisms in $BaTiO_3$-$BiMO_3$ ceramics. J Am Ceram Soc 2018, **101**: 2376-2390.

[31] Yao J, Liu F, Wang X, et al. Enhancing comprehensive properties of HVOF thermally sprayed WC-10Co coatings using two grain inhibitors. Surf Coat Technol 2024, **477**: 130323.

[32] Dong Y, Zhang D, Li D, et al. Control of ostwald ripening. Sci China Mater 2023, **66**: 1249-1255.

[33] Piwonski I, Spilarewicz-Stanek K, Kisielewska A, et al. Examination of ostwald ripening in the photocatalytic growth of silver nanoparticles on titanium dioxide coatings. Appl Surf Sci 2016, **373**: 38-44.

[34] Li H, Zheng Z, Zheng L, et al. Superior hydrogen permeation resistance in ultrathin oxide nanofilm via crystalline/amorphous interface design. Scr Mater 2025, **264**: 116703.

[35] Li Q, Wang J, Xiang Q, et al. Novel nano-crystalline Er_2O_3 hydrogen isotopes permeation barriers. J Eur Ceram Soc 2017, **37**: 249-254.

[36] Yang H, Shao Z, Wang W, et al. A composite coating of GO-Al_2O_3 for tritium permeation barrier. Fusion Eng Des 2020, **156**: 111689.

[37] Wang W, Yu Q, Liu X, et al. Preparation of Al_2O_3/Y_2O_3 composite coating for deuterium permeation reduction. J Rare Earths 2020, **38**: 1237-1242.

[38] Rai S, Rayjada PA, Dhorajiya PB, et al. Deuterium permeation studies through bare and Er_2O_3 coated SS 316L. Fusion Eng Des 2024, **206**: 114587.

[39] Wu Y, He D, Li S, et al. Deuterium permeation properties of Y_2O_3/Cr_2O_3 composite coating prepared by MOCVD on 316L stainless steel. Int J Hydrog Energy 2016, **41**: 7425-7430.

[40] Zhang G, Han W, Zhang L, et al. Preparation and deuterium permeation properties of Ti/AlN/Ti/AlN multiple coatings. Rare Metal Mat Eng 2022, **51**: 3943-3948.

[41] Wu Y, Jiang L, He D, et al. Effect of Cr_2O_3layer on the deuterium permeation properties of Y_2O_3/Cr_2O_3 composite coating prepared by MOCVD. Int J Hydrog Energy 2016, **41**: 16101-16107.

[42] Wu Y, He D, Li S, et al. Effect of microstructure change on the deuterium permeation properties of erbium oxide coatings prepared via MOCVD. Int J Hydrog Energy 2016, **41**: 431-438.

[43] Wu Y, Zhu S, Zhang Y, et al. The adhesion strength and deuterium permeation property of SiC films synthesized by magnetron sputtering. Int J Hydrog Energy 2016, **41**: 10827-10832.

[44] Tian X, Li H, Zheng L, et al. Effect of Cr_2O_3 nanosheet insertion on the deuterium permeation behavior of a Cr-Zr-O coating. Plasma Sci Technol 2022, **24**: 124017.

[45] Xiang X, Zhang G, Yang F, et al. Cr effect on hydrogen interactions with intrinsic point defects and hydrogen diffusion in α-Al_2O_3 as tritium permeation barriers. J Phys Chem C 2016, **120**: 9535-9544.

[46] Sidelev DV, Kashkarov EB, Syrtanov MS, et al. Nickel-chromium (Ni-Cr) coatings deposited by magnetron sputtering for accident tolerant nuclear fuel claddings. Surf Coat Technol 2019, **369**: 69-78.

[47] Xie Z, Wang Y, Lu C, et al. Sluggish hydrogen diffusion and hydrogen decreasing stacking fault energy in a high-entropy alloy. Mater Today Commun 2021, **26**: 101902.

[48] Moshtaghi M, Safyari M, Mori G. Hydrogen absorption rate and hydrogen diffusion in a ferritic steel coated with a micro- or nanostructured ZnNi coating. Electrochem Commun 2022, **134**: 107169.

[49] Zhou P, Li W, Liu B, et al. Communication-hydrogen permeation resistance of nickel coating enhanced by adding the rare earth element Ce. J Electrochem Soc 2017, **164**: D1042-D1044.

[50] Du Y, Wang X N, Du Z W et al. Hydrogen diffusivity in dislocation, grain boundary, and lattice of α-Fe based on electrochemical hydrogen permeation experiments and Maxwell–Garnett calculations. Corros Sci 2024, **233**: 112089.

[51] Oudriss A, Creus J, Bouhattate J et al. Grain size and grain-boundary effects on diffusion and trapping of hydrogen in pure nickel. Acta Mater 2012, **19**: 6814-6828.

[52] Sun F, Liu Q, Xu B et al. Trapping and de-trapping behavior of hydrogen isotopes in <100> interstitial dislocation loops of tungsten. Nucl Fusion 2025, **7**: 76010.

[53] Moshtaghi M, Safyari M, Mori G. Combined thermal desorption spectroscopy, hydrogen visualization, HRTEM and EBSD investigation of a Ni-Fe-Cr alloy: The role of hydrogen trapping behavior in hydrogen-assisted fracture. Mat Sci Eng a-

Struct 2022, **848**: 143428.

[54] Qian F, Cao D, Chen S et al. High-entropy RuO_2 catalyst with dual-site oxide path for durable acidic oxygen evolution reaction. Nat Commun 2025, **16**: 6894.

[55] Liu P, Zhang B, Niu R et al. Engineering metal-carbide hydrogen traps in steels. Nat Commun 2024, **15**: 724.

[56] Hu L, Zhong F, Zhang J, et al. High hydrogen isotopes permeation resistance in (TiVAlCrZr)O multi-component metal oxide glass coating. Acta Mater 2022, **238**: 118204.

[57] Ramaniah LM. First principles DFT investigation of yttrium-decorated boron-nitride nanotube: electronic structure and hydrogen storage. AIP Conf Proc 2015, **1665**: 050115.

[58] Wang C, Han K, Liu X, et al. First-principles study of hydrogen-vacancy interactions in CoCrFeMnNi high-entropy alloy. J Alloy Compd 2022, **922**: 166259.